Giant birefringence in optical antenna arrays with widely tailorable optical anisotropy

Mikhail A. Kats[a], Patrice Genevet[a,b], Guillaume Aoust[a,c], Nanfang Yu[a], Romain Blanchard[a], Francesco Aieta[a,d], Zeno Gaburro[a,e], and Federico Capasso[a,1]

[a]School of Engineering and Applied Sciences, Harvard University, Cambridge, MA 02138; [b]Institute for Quantum Studies and Department of Physics, Texas A&M University, College Station, TX 77843; [c]Department of Physics, Ecole Polytechnique, 91128 Palaiseau Cedex, France; [d]Dipartimento di Scienze e Ingegneria della Materia, dell'Ambiente ed Urbanistica Università Politecnica delle Marche, via Brecce Bianche, 60131 Ancona, Italy; and [e]Dipartimento di Fisica, Università degli Studi di Trento, via Sommarive 14, 38100 Trento, Italy

Contributed by Federico Capasso, June 22, 2012 (sent for review May 3, 2012)

The manipulation of light by conventional optical components such as lenses, prisms, and waveplates involves engineering of the wavefront as it propagates through an optically thick medium. A unique class of flat optical components with high functionality can be designed by introducing abrupt phase shifts into the optical path, utilizing the resonant response of arrays of scatterers with deeply subwavelength thickness. As an application of this concept, we report a theoretical and experimental study of birefringent arrays of two-dimensional (V- and Y-shaped) optical antennas which support two orthogonal charge-oscillation modes and serve as broadband, anisotropic optical elements that can be used to locally tailor the amplitude, phase, and polarization of light. The degree of optical anisotropy can be designed by controlling the interference between the waves scattered by the antenna modes; in particular, we observe a striking effect in which the anisotropy disappears as a result of destructive interference. These properties are captured by a simple, physical model in which the antenna modes are treated as independent, orthogonally oriented harmonic oscillators.

plasmonics | resonance | metasurfaces | scattering

The general function of optical devices consists of the modification of the wavefront of light by altering its phase, amplitude, and polarization in a desired manner. The class of optical components with varying phase retardation includes lenses, waveplates, spiral phase plates (1), axicons (2), and more generally spatial light modulators, which are able to imitate many of these components by means of a dynamically tunable spatial response (3). All of these conventional optical components rely on gradual evolution of phase, amplitude, and polarization as the wave propagates through an optically thick medium. The introduction of abrupt phase changes into the optical path by using the resonant behavior of plasmonic nanostructures allows one to achieve control over the wavefront without relying on gradual phase accumulation (4). This approach is now enabling the design of various optical devices which are thin compared to the wavelength of light (5–7).

Our previous work on phase discontinuities involved spatially inhomogeneous configurations of V-shaped optical antennas (4, 5, 7). Here, we report that homogeneous arrays optical antennas supporting two independent and orthogonally oriented current modes operate as highly birefringent meta-surfaces. We consider arrays of V-shaped antennas, creating a connection with our previous work, and Y-shaped antennas in which the anisotropy can be widely tailored or extinguished via interference between the scattered light from the two current modes. A simple, analytical two-oscillator model for such two-dimensional (2D) optical antennas is developed which captures the physics of these antennas and provides an intuitive way to understand how engineering of the amplitude and phase of the scattered light provides control over the optical anisotropy of the resulting meta-surface.

Model

Two-Dimensional Optical Antennas as Double Oscillators. The optical response of surface plasmons in confined structures such as optical antennas is well-described in terms of a charge-oscillator model that includes the effects of forcing by the incident electric field, internal damping, and radiation reaction (8). Of particular interest for this study are 2D optical antennas because they support orthogonal, independent current modes. By controlling their dimension and shape, their inherent optical anisotropy can be tailored over a broad range. In this section, we develop an extension of the charge-oscillator model for V-shaped optical antennas, which can serve as elements of birefringent meta-surfaces. Examples of other, previously investigated 2D plasmonic structures which support orthogonal modes include asymmetric cross antennas (9), L-shaped nanoparticles and antennas (10, 11), split rings (12), and rectangular patch antennas (13).

Treating the two plasmonic modes as independent harmonic oscillators, the combined system can be represented as two charged masses on orthogonally oriented springs (schematics in Fig. 1 *A* and *B*). The two oscillators are oriented along x and along y, respectively, with the incident light propagating along z and its electric field oriented along an axis w, which lies in the x-y plane at an angle θ from the y axis (Fig. 1*C*). For a charged, driven oscillator oriented along the x axis, the complex amplitude $x(\omega)$ of the displacement from the equilibrium position, assumed to be harmonically varying as $x(\omega)\ e^{i\omega t}$, can be written as (8):

$$x(\omega) = \frac{\frac{q_x}{m_x}E_{0,x}}{({\omega_{0,x}}^2 - \omega^2) + i\frac{\omega}{m_x}(\Gamma_{a,x} + \omega^2\Gamma_{s,x})} = \tilde{x}(\omega)E_{0,x}, \qquad [1]$$

where q_x is the participating charge, m_x is the mass, $\omega_{0,x}$ is the resonant frequency, and $\Gamma_{a,x}$ and $\Gamma_{s,x}$ are the damping coefficients representing absorption and scattering, respectively. The field emitted by the oscillator $E_{s,x}(\omega)$ can be written as

$$E_{s,x}(\omega) = -D_x(\mathbf{r})\sqrt{\Gamma_{s,x}}\omega^2 x(\omega). \qquad [2]$$

In Eq. **2**, $D_x(\mathbf{r})$ contains the angular and radial dependence of the emitted field. The exact form of $D_x(\mathbf{r})$ depends on the specific geometry of the oscillator and the surrounding environment, but in the limit that the oscillator element is small relative to the wavelength of light, $D_x(\mathbf{r})$ is simply the emission pattern of a radiating electric dipole (*SI Text*). The expressions for the y-oscillator [$y(\omega)$, $\tilde{y}(\omega)$ and $E_{s,y}(\omega)$] are analogous to that of the x-oscillator.

Author contributions: M.A.K. designed research; M.A.K., P.G., and G.A. performed research; F.C. supervised research; M.A.K., P.G., N.Y., R.B., F.A., Z.G., and F.C. analyzed data; and M.A.K., P.G., N.Y., R.B., Z.G., and F.C. wrote the paper.

The authors declare no conflict of interest.

Freely available online through the PNAS open access option.

[1]To whom correspondence should be addressed. E-mail: capasso@seas.harvard.edu.

This article contains supporting information online at www.pnas.org/lookup/suppl/doi:10.1073/pnas.1210686109/-/DCSupplemental.

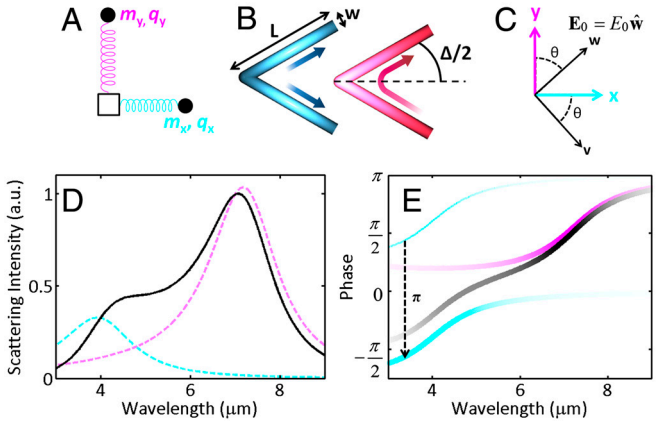

Fig. 1. (*A*) Charge-oscillator model of a two-mode plasmonic element, where q_i are the charges and m_i are the inertial masses. (*B*) A metallic V-shaped antenna which supports two orthogonal charge-oscillation modes (blue and pink). The arrows show the direction of current flow, and the colors represent the current density (lighter color indicates higher current). The axis of symmetry is marked with a dashed line. (*C*) Two coordinate systems related via rotation by angle θ. The *x*-*y* axes are along the two fundamental oscillator modes, the *w* axis is along the polarization of the incident field $\mathbf{E}_0$, and the *v* axis is along the cross-polarized component of the emitted field. (*D*) Calculated intensity $|E|^2$ of the field scattered into the cross-polarization by the two individual oscillators representing, in this case, two modes of a V-shaped antenna (blue and pink) with $\Delta = 90°$ and $L = 650$ nm, and by the combined system (black) for $\theta = 45°$. Note that the black curve is not simply the sum of the blue and pink curves because of the coherent addition of fields. (*E*) Phase of the field scattered into the cross-polarization by the individual oscillators (blue and pink), and by the combined system (black). The brightness of the color encodes the scattering intensity, with darker colors signifying more intense scattering. The blue curve (due to the *x*-oscillator) is shifted down by π from its intrinsic oscillator phase due to the geometry (see last term in Eq. **5**).

In general, light is scattered by the two-oscillator element into some elliptical polarization. Deliberate engineering of this polarization state offers intriguing prospects, but remains outside of the scope of this work. Instead, we focus on light scattered into the polarization state along the *v* axis in Fig. 1*C*, which is the cross-polarized direction relative to the incident light. The polarization conversion efficiency is a direct measure of the degree of anisotropy of the 2D plasmonic antenna, and can be easily isolated by filtering out light with the incident polarization with a linear polarizer. This cross-polarized configuration is also critical for the design of planar optical components, as it extends the phase coverage of the scatterers to cover a full 2π range (4).

Given an incident field polarized along $\hat{w}$, (Fig. 1*C*), we calculate the component of the emitted field polarized along the *v* direction $E_{s,v}(\omega)$. We can break up this polarization-conversion process into two steps: the in-coupling of incident light into the two oscillator modes, and the out-coupling of cross-polarized light. The in-coupling process involves the projection of the incident field along the two oscillator modes, which can be expressed as $E_{0,x} = E_0\hat{w}\cdot\hat{x} = E_0\sin(\theta)$ and $E_{0,y} = E_0\hat{w}\cdot\hat{y} = E_0\cos(\theta)$. For the out-coupling process, we project the field scattered by each oscillator onto the *v* axis to arrive at

$$E_{s,x}\hat{v}\cdot\hat{x} = -D_x(\mathbf{r})\sqrt{\Gamma_{s,x}}\omega^2\tilde{x}(\omega)E_{0,x}\cos(\theta) \quad [3]$$

$$E_{s,y}\hat{v}\cdot\hat{y} = D_y(\mathbf{r})\sqrt{\Gamma_{s,y}}\omega^2\tilde{y}(\omega)E_{0,y}\sin(\theta). \quad [4]$$

After summing these projections, the total cross-polarized field emitted by the structure $E_{s,v}$ can be written as

$$E_{s,v}(\omega) = D(\mathbf{r})\frac{E_0}{2}\sin(2\theta)\omega^2[\sqrt{\Gamma_{s,x}}\tilde{x}(\omega)e^{i\pi} + \sqrt{\Gamma_{s,y}}\tilde{y}(\omega)], \quad [5]$$

where we assumed that $D_x(\mathbf{r}) \approx D_y(\mathbf{r}) = D(\mathbf{r})$, which is true for light emitted approximately normal to the orientation of the two oscillators. Eq. **5** provides a complete description of the generation of cross-polarized light by our two-oscillator system. The intensity $|E_{s,v}(\omega)|^2$ and phase $\varphi(\omega)$ of the cross-polarized light $[E_{s,v}(\omega) = |E_{s,v}(\omega)|e^{i\varphi(\omega)}]$ are plotted in Fig. 1 *D* and *E*. The specific parameters $\Gamma_{a,i}$, $\Gamma_{s,i}$, m_i, $\omega_{0,i}$ $(i \in x, y)$ for the two oscillators used in generating Fig. 1 *D* and *E* correspond roughly to the modes of a typical isolated V-shaped antenna (*SI Text*).

The phase of the cross-polarized light generated by our two-oscillator element (black curve in Fig. 1*E*) is able to span twice the range of phase of either single oscillator (blue or pink), even though the two oscillators are uncoupled and operate independently. This phase extension, which can be seen as the $e^{i\pi}$ term in Eq. **5**, is due to the fact that the projections of the scattered fields from the spatially overlapped *x*- and *y*-oriented oscillators onto the *v* axis are opposite in phase (Fig. 1*C* and Eqs. **3** and **4**), and is shown graphically in Fig. 1*E* as a shift of the intrinsic phase response of the *x*-oscillator (blue curve) down by π. As a result, this two-oscillator system is able to provide much larger phase coverage in cross-polarization while maintaining a significant scattering amplitude. The use of two spectrally separate resonances as in Fig. 1 allows one to broaden the frequency range over which there is significant polarization conversion (Fig. 1*D*), creating broadband optical anisotropy.

Eq. **5** encodes the θ-dependence of the polarization conversion properties with the $\sin(2\theta)$ term. No cross-polarized light is generated for $\theta = 0°$ or 90° when the incident field is aligned along one of the two orthogonally oriented oscillators, and maximum polarization conversion is obtained for $\theta = 45°$. Because of the $\sin(2\theta)$ dependence, a rotation of the structure by 90° maintains the amplitude of cross-polarized scattering while adding an extra phase of π to the scattered light. This feature of double oscillators allows for the same element to scatter with phase φ and $\varphi + \pi$, simply by applying a 90° rotation ($\theta' = \theta + 90°$ in Eq. **5**), and was used in ref. (4) to generate eight distinct phase elements from four V-shaped antennas.

The intensity and phase response of cross-polarized scattered light in Fig. 1 *D* and *E* is given as a function of wavelength (or, equivalently, frequency) for a fixed set of oscillator parameters. However, a careful analysis of Eq. **1** leads to an alternative approach; because Eq. **1** depends on $(\omega_0^2 - \omega^2)$, one can plot the amplitude and phase response of an oscillator as a function of ω_0 for a fixed frequency ω. This method of analyzing the behavior of oscillators is required for the design of phase elements for single-frequency optical components (4, 5, 14). These two approaches are complementary; if wide tunability of the phase response for a fixed oscillator (or set of oscillators) is achieved as a function of frequency, then it can likewise be achieved for a fixed operating frequency by exploring the parameter space of the oscillator.

Results and Discussion

Broadband Spectral and Polarization-Conversion Properties of V-Antenna Arrays. To experimentally characterize the birefringent properties of meta-surfaces based on V-shaped antennas, we performed mid-IR measurements of arrays fabricated by electron-beam lithography (see SEM in Fig. 2) using an FTIR spectrometer. In Fig. 2 *A* and *B* we plot the measured $(1 - T)$ spectra, where T is the transmission through arrays of V-shaped gold antennas ($L \approx 650$ nm, $w \approx 130$ nm, Si substrate) for opening angles Δ from 45° to 180° at normal incidence. The quantity $(1 - T)$ corresponds to the sum of the scattering and absorption spectra, and is sometimes referred to as extinction. The incident polarization was fixed along the *x* and *y* directions in *A* and *B*, respectively.

The $(1 - T)$ spectra peak around the resonance frequencies of the antenna modes, and the expected small differences between the spectral locations of the scattering and absorption

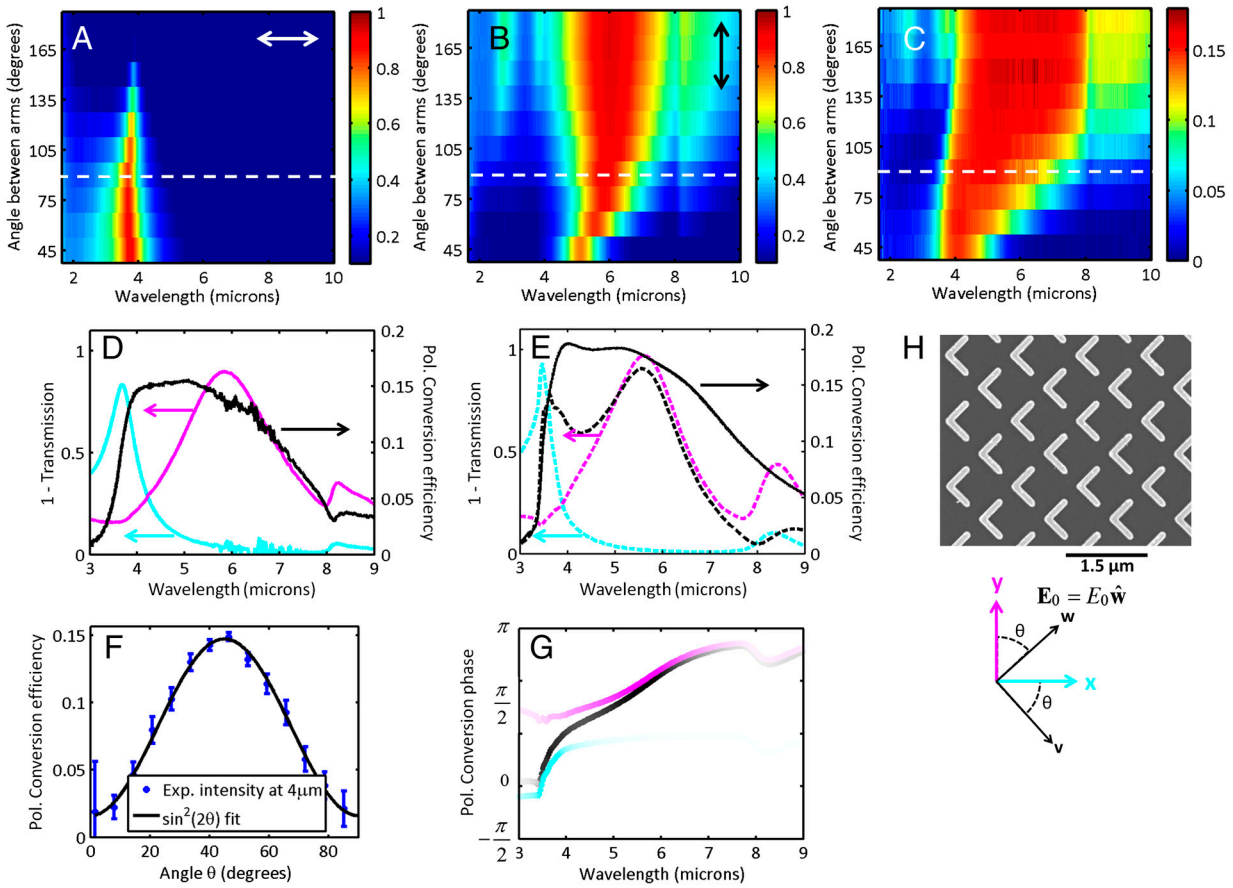

Fig. 2. (*A*, *B*). Color maps showing the measured extinction (defined as 1 – Transmission) spectra through arrays of lithographically-defined V-antennas ($L \simeq 650$ nm, Δ from 45° to 180°) for *x*- and *y*-oriented incident polarizations, respectively. (*C*) Color map showing the polarization conversion efficiency spectra when the incident field is polarized at a $\theta = 45°$ angle between both principle axes. (*D*) Blue and pink curves are the measured extinction through the V-antenna array with $\Delta = 90°$ for the *x*-oriented (blue) and *y*-oriented (pink) incident polarization for every antenna. The black curve is the polarization conversion efficiency for $\theta = 45°$. The three curves correspond to line scans of *A*–*C*, shown by the white dashed lines. (*E*) FDTD simulations corresponding to the curves in *D*, with the dashed curves representing simulations with an infinitely thick substrate and the solid black curve representing the calculated polarization-conversion efficiency when the finite (280 μm) thickness of the substrate is accounted for. (*F*) Measured polarization conversion efficiency at $\lambda = 4$ μm plotted vs. the incident polarization angle θ (blue symbols) and a fit to a $\sin^2(2\theta)$ dependence as predicted by Eq. **5**. The calculated correlation *R* is 0.997. (*G*) Phase response of the cross-polarized light generated by the antennas as calculated by FDTD (black). The blue and pink curves represent the phases of the contributions from the symmetric and antisymmetric modes, respectively. Brightness of the phase curves indicates the intensity of the scattered light. (*H*) SEM image of the $\Delta = 90°$ V-antenna array and the coordinate system.

peaks (8) are obscured by the inhomogeneities of the arrays. The first-order approximation of the locations of the two peaks yields $\lambda_{0,x} \simeq 2Ln_{\text{eff}} = 3.4$ μm and $\lambda_{0,y} \simeq 4Ln_{\text{eff}} = 6.8$ μm, taking n_{eff} as 2.6 (4). The measurements yield slightly different values ($\lambda_{0,x} \simeq 3.7$ μm and $\lambda_{0,y} \simeq 6$ μm for $\Delta = 90°$, e.g.) due to the nonzero thickness and width of the antennas, coupling between neighboring elements, and the presence of native oxide on the silicon surface (approximately 2 nm as measured by ellipsometry), which is also responsible for the sharp feature at approximately 8–8.5 μm (15, 16) (*SI Text*). The spectral position of the resonances shifts with varying Δ due to near-field interactions between the two arms, which are strongest for small Δ. In Fig. 2*C*, we plotted the power of the generated cross-polarized beam, normalized to the incident light, when the polarization is along $\theta = 45°$, where θ is defined in Fig. 1*C*. As expected, the polarization conversion efficiency peaks in the 3–8 μm range, in the vicinity of the antenna resonances. In Fig. 2*D*, we plotted the line scans of Fig. 2 *A*–*C* for $\Delta = 90°$, indicated by the white dashed lines. The small, irregular oscillations between 4.5 and 7.5 μm correspond to atmospheric absorption from ambient water vapor. The corresponding finite-difference time-domain (FDTD) simulations are shown in Fig. 2*E*. Note that our choice of $\Delta = 90°$ is purely arbitrary and one can generate similar plots for any opening angle. Also note that in the experiment the substrate is a 280-μm-thick double-side polished silicon wafer; however, it is computationally intensive to include this large, finite slab in the simulations due to the high resolution required to model the nanoscale antennas. The polarization-conversion result shown as the black curve in Fig. 2*E* is a result of such a complete simulation and matches very well the experimental measurements, but all of the other simulations presented in this article are performed using an infinite silicon substrate. (see *SI Text* for more details, as well as for simulations corresponding to Fig. 2 *A*–*C*).

In Fig. 2*F*, we plot the measured polarization-conversion efficiency at $\lambda = 4$ μm (wavelength chosen to be away from the atmospheric absorption resonances) as a function of θ. The error bars account for polarizer misalignment $\Delta\theta$ and spectrometer noise. The data was fit to $A\sin^2(2\theta) + C$ to account for the θ-dependence of Eq. **5** and some offset due to imperfect cross-polarization extinction of our polarizers (black curve). Because within the 0–90° range the θ-dependence only affects the amplitude of $E_{s,y}$, θ can be used as a degree of freedom to control the cross-polarized scattering amplitude without altering its phase response (for example, simply rotating the individual elements of a planar optical component such as the vortex plates in ref. (5) allows for independent amplitude control of each antenna, enabling the

creation of a simultaneous amplitude and phase plate). The phase of the cross-polarized light (which is independent of θ) is calculated via FDTD simulations, and plotted as the black curve in Fig. 2*G*. As in Fig. 1*E*, the brightness of the curve encodes the intensity of the scattered light.

Although the intensity and phase response in Fig. 2 *D*, *E*, and *G* is given as a function of wavelength, a complementary plot can be made keeping the wavelength constant and sweeping across the arm length L because the resonant wavelengths of both oscillator modes $\lambda_{0,x}$ and $\lambda_{0,y}$ depend linearly on L, though an extra scaling factor has to be introduced in the near-IR and visible regimes (17). It is much more difficult to generate such plots because a new sample has to be fabricated and measured (or simulated) for every possible value of L; however, the *SI Text* includes approximate intensity and phase response maps for V-antennas as a function of geometrical parameters L and Δ, keeping the frequency constant.

Tailorable Optical Anisotropy via Interference in Y-Shaped Antennas. The spectral position of V-antenna resonances can be tuned by varying the arm length L and, to a smaller extent, by adjusting the opening angle Δ (Fig. 1 *A* and *C*). However, both of these simultaneously shift the resonance frequencies of the *x*-oriented (symmetric) and *y*-oriented (antisymmetric) modes of the antenna. By appending a tail of length L_T to the V-antenna as shown in Fig. 3*A*, an additional degree of freedom is attained that allows for independent tuning of the spectral position of the *x*-oriented mode. By increasing L_T, the *x*-oriented mode is red-shifted without affecting the *y*-oriented mode. We fabricated such Y-shaped antennas on a silicon substrate, with an SEM image of the structures shown in Fig. 3*A*. The *x*- and *y*-oriented modes are identified in Fig. 3 *B* and *C*, respectively, for four different values of L_T, by measuring the reflectivity spectra from arrays of these antennas. The *x*-oriented mode increases in resonant wavelength and amplitude as L_T increases, because the effective antenna length is increasing, increasing q_x, m_x, and $\Gamma_{s,x}$ and decreasing $\omega_{0,x}$ (Fig. 3*B*). The *y*-oriented mode is not perturbed by this tail section, so all of the reflectivity curves in Fig. 3*C* overlap.

The polarization conversion efficiency due to the Y-antennas is plotted in Fig. 3*D* as a function of wavelength, given incident polarization along $E_0\hat{w}$ for $\theta = 45°$ as in Figs. 1 and 2, such that the projections of the incident field along the two antenna modes are equal, which maximizes the conversion. There is a substantial amount of polarization conversion for $L_T \simeq 100$ nm, 300 nm, and 700 nm (red, black, and blue curves, respectively). However, for $L_T \simeq 500$ nm (green curve), the polarization conversion is almost completely extinguished. FDTD simulations corresponding to Fig. 3 *B*–*D* are shown in Fig. 3 *F*–*H*, and demonstrate the same behavior as in the measurements (unlike the simulations in Fig. 2 *B* and *D*, we did not include the native oxide layer in the simulations as it detracts from visual clarity, so the feature at $\lambda \sim 8$ μm is not reproduced in these simulation results). The origin of this effect can be interpreted as destructive interference between the contributions to the cross-polarization generation from the two oscillator modes. As illustrated in Fig. 3*E*, the incident field excites both the *x*-oriented and *y*-oriented modes of the Y-antenna, each of which contribute to the cross-polarized field. However, the projections of the scattering of the *x*- and *y*-oriented oscillators onto the *v* axis are opposite in phase (Fig. 1*C*), which results in an additional dephasing of π between the two contributions ($e^{i\pi}$ term in Eq. **5**).

When the two oscillators are nearly identical in their individual amplitude and phase response (as is the case for $L_T \simeq 500$ nm), their contributions to the polarization conversion efficiency are π out of phase, resulting in destructive interference (see *SI Text* for a detailed discussion). The observed imperfect extinction and line shape asymmetry are a result of the two eigenmodes in our experiment being not completely identical in linewidth, amplitude,

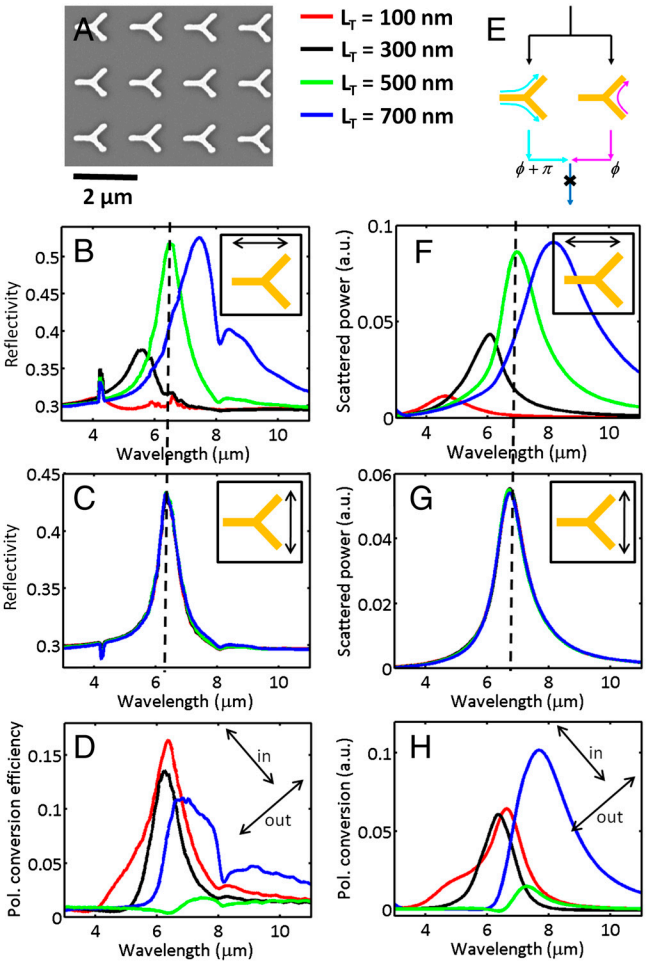

Fig. 3. Y-shaped plasmonic antennas. (*A*) SEM image of the antenna array. (*B*, *C*) Measured normal-incidence reflectivity spectra of the *x*- and *y*-oriented antenna modes, respectively, as a function of tail length L_T, which varies from 100 to 700 nm by increments of 200 nm (see *Inset*). The reflectivity of the bare silicon substrate is approximately 0.3. The vertical dashed line shows that for $L_T \simeq 500$ nm (green curves), the *x*- and *y*-oriented resonances are overlapping. The arrows indicate the polarization of the incident field. (*D*) Polarization conversion spectrum with $\theta = 45°$, with the incident and measured polarizations indicated with arrows. The polarization conversion is nearly extinguished for one intermediate value of L_T (green). (*E*) Diagram explaining the extinguishing of polarization conversion due of destructive interference between contributions of the two antenna modes when L_T is adjusted such that the two oscillator modes have the same resonant response. (*F*–*H*) FDTD simulations corresponding to the measurements in *B*–*D*. The native oxide layer was not included in the simulations for visual clarity.

and resonance frequency. In this way, Eq. **5** explains that any structure with, for example, threefold (C_3) or fourfold (C_4) rotational symmetry cannot be used for polarization conversion, and is therefore isotropic. Conversely, arrays of resonant structures which support two unequal eigenmodes can be viewed as metasurfaces with giant birefringence because they can rotate the polarization of light over a thickness of just approximately 50 nm at mid-IR wavelengths. Such birefringence arising because of structural anisotropy instead of intrinsic crystal properties of a material is sometimes referred to as "form birefringence" in literature [see, e.g., refs. (9, 11, 18–22)]. On the other hand, arrays of C_3-symmetric structures including Y-shaped antennas with equal arms (and $\Delta = 120°$) and nanoparticle trimers (23) have an isotropic in-plane response (24), and thus have no polarization-converting properties. We note that resonant metallic structures which exhibit large optical activity have been explored in the literature [e.g., refs. (25, 26)], and serve as the circular-polariza-

tion equivalents to the birefringent metallic structures demonstrated presently.

Conclusion

We showed that an optical element consisting of two orthogonally oriented uncoupled oscillators possesses widely tailorable optical anisotropy, and is able to independently control the phase and amplitude of light scattered into the cross-polarization. To demonstrate this concept, we utilized the double resonances of V- and Y-shaped plasmonic antennas. The properties of these resonances are controlled by changing the opening angle and length of the arms of both the V- and Y-shaped antennas. Though the Y-shaped antennas have a larger geometrical footprint than their V counterparts, they allow for more direct tailoring of the two eigenmodes and thus are more flexible components of anisotropic interfaces. The phase response of the individual modes in Y-shaped antennas was experimentally investigated via an interference experiment, in which the polarization conversion was extinguished by destructive interference between the contributions from two nearly identical oscillator modes. Arrays of these antennas form meta-surfaces with widely tailorable birefringence.

The approach of molding waves with both uniform and spatially varying arrays of antennas is applicable to a large part of the electromagnetic spectrum from radio frequencies to the ultraviolet. The possibility of using other optical oscillators, such as quantum dots, nanocrystals, resonant molecules, or metamolecules is promising for creating isotropic or birefringent optical phase and amplitude elements with deeply subwavelength dimensions, reduced losses, and dynamic tunability.

Methods

Fabrication. The antenna arrays were fabricated on high resistivity (>10,000 Ω-cm) double side polished silicon using a conventional electron-beam (e-beam) lithography process with lift-off. A double layer of poly (methyl methacrylate) (PMMA) resist (495A4, then 950A2; MicroChem) was spun at 4,000 rpm onto the silicon wafer, baked at 120 °C, and then exposed using a 100 kV e-beam system (Elionix ELS-7000). After development with 3:1 isopropanol:methyl isobutyl ketone (IPA:MIBK), 10 nm of titanium, and 40 nm of gold was deposited using e-beam evaporation, and the lift-off process was completed in acetone with ultrasonic agitation. For SEM images of the resulting structures, see Figs. 2*A*, 3*A*, and *SI Text*.

Measurements. The transmission and polarization conversion measurements were performed using a Bruker Vertex 70 FTIR spectrometer connected to a Hyperion 2000 mid-IR microscope. A linearly polarized Globar source is used, and the beam is focused onto the sample and is then collected in transmission mode using two 15 × objectives (N.A. = 0.4). An additional polarizer was placed between the sample and the out-coupling objective for the polarization conversion measurements and is used to isolate the scattered light into the cross-polarization. For transmission measurements, the measured signal through V- and Y-antennas on an Si substrate was normalized to the transmission through the Si substrate alone. For polarization conversion measurements, the normalization reference was taken by doing a transmission measurement through the bare Si substrate with both polarizers aligned. The uncertainty in the measurement of the spectrum away from atmospheric noise was approximately 3%, and the uncertainty in θ (polarizer alignment) was approximately 2°. These uncertainties were combined using standard error propagation to obtain the error bars in Fig. 2*C*.

Simulations. The FDTD simulations were performed using Lumerical Solutions FDTD running on a workstation. For Fig. 2 *B* and *D*, the transmission and cross-polarization properties of V-antenna arrays were simulated by using periodic boundary conditions to define a single repeating unit cell of (1 μm × 1 μm), each containing a single antenna. A broadband planewave was launched from the silicon side to illuminate the antenna array. The phase response in Fig. 2*D* was obtained by performing a near- to far-field transform and looking at a point 1 m above the antenna array in a direction normal to the surface. The phase response was calculated as the phase of the field at that point less the phase accumulated by the plane wave via propagation through the silicon slab and the air above the array. For Fig. 3 *F–H*, the simulations of the Y-antennas were done by defining a 3 × 3 array of antennas at a spacing of 1.7 μm × 1.7 μm, and using a total-field scattered-field (TFSF) plane wave source with perfectly matched layer (PML) boundary conditions (see *SI Text* for more details).

ACKNOWLEDGMENTS. The authors acknowledge helpful discussions with Jonathan Fan, and support from the National Science Foundation (NSF), Harvard Nanoscale Science and Engineering Center (NSEC) under contract NSF/PHY 06-46094, and the Center for Nanoscale Systems (CNS) at Harvard University. This work was supported in part by the Defense Advanced Research Projects Agency (DARPA) Nano- and Micro-Electro-Mechanical Systems (N/MEMS) Science and Technology (S&T) Fundamentals program under grant N66001-10-1-4008 issued by the Space and Naval Warfare Systems Center Pacific (SPAWAR). M. Kats is supported by NSF through a Graduate Research Fellowship. P. Genevet acknowledges support from the Robert A. Welch Foundation (A-1261). Z. Gaburro acknowledges funding from the European Communities Seventh Framework Programme (FP7/2007–2013) under grant agreement PIOF-GA-2009-235860. Harvard CNS is a member of the National Nanotechnology Infrastructure Network (NNIN).

1. Watanabe T, Fujii M, Watanabe Y, Toyama N, Iketaki Y (2004) Generation of a doughnut-shaped beam using a spiral phase plate. *Rev Sci Instrum* 75:5131–5135.
2. McLeod JH (1954) The axicon—A new type of optical element. *J Opt Soc Am* 44:592–597.
3. Casasent D (1977) Spatial light modulators. *Proc IEEE* 65:143–157.
4. Yu N, et al. (2011) Light propagation with phase discontinuities: Generalized laws of reflection and refraction. *Science* 334:333–337.
5. Genevet P, et al. (2012) Ultra-thin plasmonic optical vortex plate based on phase discontinuities. *Appl Phys Lett* 100:013101.
6. Ni X, et al. (2012) Broadband light bending with plasmonic nanoantennas. *Science* 335:427.
7. Aieta F, et al. (2012) Out-of-plane reflection and refraction of light by anisotropic optical antenna metasurfaces with phase discontinuities. *Nano Lett* 12:1702–1706.
8. Kats MA, Yu N, Gaburro Z, Genevet P, Capasso F (2011) Effect of radiation damping on the spectral response of plasmonic components. *Opt Express* 19:21748–21753.
9. Biagioni P, et al. (2009) Near-field polarization shaping by a near-resonant plasmonic cross-antenna. *Phys Rev B* 80:153409.
10. Xu Q, et al. (2007) Fabrication of large-area patterned nanostructures for optical application by nanoskiving. *Nano Lett* 7:2800–2805.
11. Sung J, et al. (2008) Nanoparticle spectroscopy: Birefringence in two-dimensional arrays of L-shaped silver nanoparticles. *J Phys Chem C* 112:3252–3260.
12. Enkrich C, et al. (2005) Magnetic metamaterials at telecommunication and visible frequencies. *Phys Rev Lett* 95:203901.
13. Esteban R, Teperik TV, Greffet JJ (2010) Optical patch antennas for single photon emission using surface plasmon resonances. *Phys Rev Lett* 104:026802.
14. Fattal D, Li J, Peng Z, Fiorentino M, Beausoleil RG (2010) Flat dielectric grating reflectors with focusing abilities. *Nat Photonics* 4:466–470.
15. Neubrech F, Weber D, Enders D, Nagao T, Pucci A (2010) Antenna sensing of surface phonon polaritons. *J Phys Chem C* 114:7299–7301.
16. Shelton DJ, et al. (2011) Strong coupling between nanoscale metamaterials and phonons. *Nano Lett* 11:2104–2108.
17. Novotny L (2007) Effective wavelength scaling for optical antennas. *Phys Rev Lett* 98:266802.
18. Kikuta H, Ohira Y, Iwata K (1997) Achromatic quarter-wave plates using the dispersion of form birefringence. *Appl Opt* 36:1566–1572.
19. Feng L, et al. (2011) Metamaterials for enhanced polarization conversion in plasmonic excitation. *ACS Nano* 5:5100–5106.
20. Shcherbakov MR, Dobynde MI, Dolgova TV, Tsai D-P, Fedyanin AA (2010) Full Poincare sphere coverage with plasmonic nanoslit metamaterials at Fano resonance. *Phys Rev B* 82:193402.
21. Gotschy W, Vonmentz K, Leitner A, Aussenegg FR (1996) Optical dichroism of lithographically defined silver nanoparticle films. *Opt Lett* 21:1099–1101.
22. Gonzalez AL, Reyes-Esqueda JA, Noguez C (2008) Optical properties of elongated noble metal nanoparticles. *J Phys Chem C* 112:7356–7362.
23. Fan JA, et al. (2010) Self-assembled plasmonic nanoparticle clusters. *Science* 328:1135–1138.
24. Brandl DW, Mirin NA, Nordlander P (2006) Plasmon modes of nanosphere trimers and quadrumers. *J Phys Chem B* 110:12302–12310.
25. Svirko Y, Zheludev N, Osipov M (2001) Layered chiral metallic microstructures with inductive coupling. *Appl Phys Lett* 78:498–500.
26. Papakostas A, et al. (2003) Optical manifestations of planar chirality. *Phys Rev Lett* 90:107404.